Generalized Inversion of n-dimensional Flux Maps for Unified Nonlinear Machine Models and Predictive Control Algorithms

Leonard Geier
Elektrotechnisches Institut (ETI)
Karlsruhe Institute of Technology (KIT)
Karlsruhe, Germany
leonard.geier@kit.edu

Johannes Stoß
Elektrotechnisches Institut (ETI)
Karlsruhe Institute of Technology (KIT)
Karlsruhe, Germany
johannes.stoss@kit.edu

Dr.-Ing. Andreas Liske
Elektrotechnisches Institut (ETI)
Karlsruhe Institute of Technology (KIT)
Karlsruhe, Germany
andreas.liske@kit.edu

Prof. Dr.-Ing. Marc Hiller
Elektrotechnisches Institut (ETI)
Karlsruhe Institute of Technology (KIT)
Karlsruhe, Germany
marc.hiller@kit.edu

***Abstract*—This paper describes a precise and fast method for inverting n-dimensional flux maps. These are necessary to fully model the nonlinearities of different machine types in a uniform and real-time capable way. With this tool, the known model predictive control methods (MPC) and simulation models for permanent magnet synchronous machines (PMSM) can be adapted to be used for a larger class of generalized machines, which includes electrically excited synchronous machines (EESM) and induction motors (IM) as well. Additional dependencies such as rotor position angle, temperature or speed can also easily be included in the map. This improves control quality and enables standardization of nonlinear controls across different machine types. In addition to that, the required memory to store such a flux map in lookup tables is significantly reduced by storing the flux map not in the dq-coordinate system, but in a coordinate system that is aligned to the magnetic couplings.**

***Index Terms*—induction motor, synchronous motor, permanent magnet motor, electrically excited synchronous machine, flux model, model-based predictive control (MPC), nonlinear control, hardware in the loop (HIL)**

I. Introduction

Today the permanent magnet synchronous machine (PMSM) is the most common motor for automotive applications due to its high power density and efficiency. To achieve a small mechanical footprint the PMSM is highly utilized in the magnetic and electric path. This results in a strong nonlinear behavior. For the PMSM the nonlinearities have been studied extensively and advanced methods for accurate machine models [1], hardware in the loop (HIL) testing [2] and control algorithms have been developed [3], [4]. They all have in common that the nonlinear behavior of the PMSM is modeled using inverse flux maps.

Recently, the interest in rare-earth-free electrical machines has increased which intensifies the drive to transfer these methods to electrically excited synchronous machines (EESM) and induction motors (IM). This requires a method to model nonlinearities in an identical way for all kinds of machines that is suitable for hard real-time conditions.

The short summary in section II describes how inverse flux maps of higher dimensions can be used for generalization of existing methods to a broader class of machines. Some fundamentals of approximating functions with maps are summarized in section III. The inversion algorithm is presented in section IV followed by the discussion of inversion results from measured datasets in section V.

II. Machine modeling using inverse flux maps

Models for electric motors are based on the voltage equations and a flux model that describes the relation between the machine's current and flux components. The simplest form of a PMSM's flux model in rotor orientation can be written as

$$\psi_\mathrm{d} = L_\mathrm{d} i_\mathrm{d} + \psi_\mathrm{PM} \tag{1}$$

$$\psi_\mathrm{q} = L_\mathrm{q} i_\mathrm{q} \tag{2}$$

where i_d, i_q are the currents, ψ_d, ψ_q the flux components, L_d, L_q the stator inductances and ψ_PM the permanent magnet flux. This simplified model no longer holds for highly utilized electric drives. For large current values iron saturation causes the flux to no longer increase proportional to the current. The mapping between each current and its respective flux component becomes highly nonlinear. In addition to that both flux components can affect each other as they share the same magnetic path in the stator yoke. Thus saturation in one component can lead to a decreased flux in the other one. This phenomenon is known as cross coupling. It requires each flux component to be modeled as a function of both currents. Hence the flux model can be expressed more precisely as a two-dimensional mapping

$$f_\psi : (i_\mathrm{d}, i_\mathrm{q}) \mapsto (\psi_\mathrm{d}, \psi_\mathrm{q}) \tag{3}$$

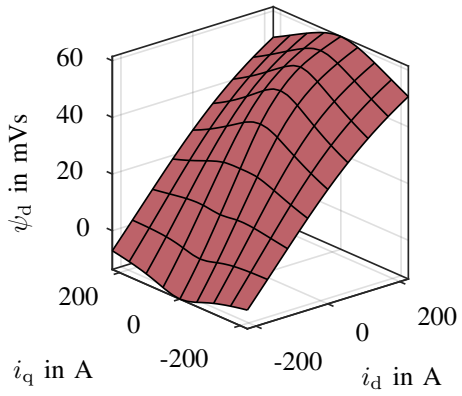

Fig. 1. d-flux of a PMSM flux map with saturation and cross coupling

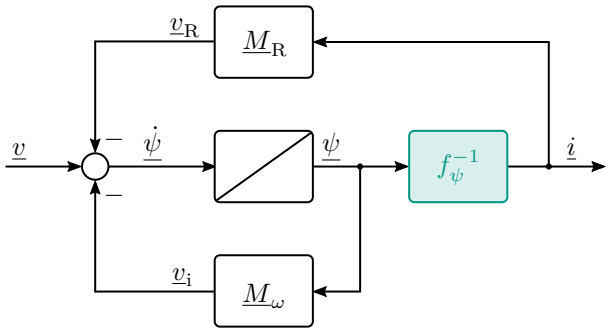

Fig. 2. Generalized Machine Model with inverse flux map (green)

that has to be determined by finite element analysis (FEA) or measurement. As an example the d-flux of a PMSM is shown in Fig 1. Both, saturation and cross coupling, are visible.

To further increase the model's accuracy more dependencies can be added to the mapping. If spatial harmonics should be included, the rotor position angle has to be added as parameter [5]. The temperature dependent remanence flux of the permanent magnets and the speed dependent effects of the iron losses can be taken into account if temperature and speed are additional parameters.

The PMSM's system dynamics is given by the voltage equations

$$v_\mathrm{d} = R_\mathrm{S} i_\mathrm{d} + \dot{\psi}_\mathrm{d} - \omega \psi_\mathrm{q} \tag{4}$$

$$v_\mathrm{q} = R_\mathrm{S} i_\mathrm{q} + \dot{\psi}_\mathrm{q} + \omega \psi_\mathrm{d} \tag{5}$$

with the stator voltages v_d, v_q the stator resistance R_S and the electrical frequency ω. These equations form a system of differential equations for the flux components. For simulation models or predictive control algorithms the system can be solved for a given input voltage. To do so the flux and current values are evaluated for discrete time points t_k. The flux at the next time step is calculated by numerically integrating its derivative as shown below for the d-flux.

$$\psi_{\mathrm{d},k+1} = \psi_{\mathrm{d},k} + \int_{t_k}^{t_{k+1}} \dot{\psi}_\mathrm{d} \mathrm{d}t \tag{6}$$

To obtain the respective current value $i_{\mathrm{d},k+1}$ the inverse flux map

$$f_\psi^{-1} : (\psi_\mathrm{d}, \psi_\mathrm{q}) \mapsto (i_\mathrm{d}, i_\mathrm{q}) \tag{7}$$

is needed. The procedure to solve the differential equations is shown as a block diagram in Fig 2. For the vector and matrix quantities the PMSM values from Table I are used.

As EESM and IM have additional state quantities, the machine dynamic and the flux model increase in dimension. For the EESM the stator dynamic is modeled analogously to the PMSM with (4) and (5). Additionally, one equation that describes the rotor dynamic is needed

$$v_\mathrm{e} = R_\mathrm{R} i_\mathrm{e} + \dot{\psi}_\mathrm{e} \tag{8}$$

where v_e, R_R, i_e and ψ_e are the voltage, resistance, current and flux of the excitation winding in the rotor respectively. Similarly one additional equation is needed to model the IM in the rotor flux oriented reference frame (RFO).

$$0\mathrm{V} = R_\mathrm{Rd} i_\mathrm{Rd} + \dot{\psi}_\mathrm{Rd} \tag{9}$$

Rotor resistance, current and flux are denoted with the index "Rd". As the rotor is short-circuited the rotor voltage is zero. In RFO the rotor q-flux is zero per definition. It has to be noted

TABLE I
PARAMETERS FOR THE GENERALIZED MACHINE MODEL

Machine Type	$\underline{v}$	$\underline{i}$	$\underline{\psi}$	$\underline{M}_\mathrm{R}$	$\underline{M}_\omega$	f_ψ
PMSM	$\begin{pmatrix} v_\mathrm{d} \\ v_\mathrm{q} \end{pmatrix}$	$\begin{pmatrix} i_\mathrm{d} \\ i_\mathrm{q} \end{pmatrix}$	$\begin{pmatrix} \psi_\mathrm{d} \\ \psi_\mathrm{q} \end{pmatrix}$	$\begin{pmatrix} R_\mathrm{S} & 0 \\ 0 & R_\mathrm{S} \end{pmatrix}$	$\begin{pmatrix} 0 & -\omega \\ \omega & 0 \end{pmatrix}$	$\begin{pmatrix} i_\mathrm{d} \\ i_\mathrm{q} \end{pmatrix} \mapsto \begin{pmatrix} \psi_\mathrm{d} \\ \psi_\mathrm{q} \end{pmatrix}$
EESM	$\begin{pmatrix} v_\mathrm{d} \\ v_\mathrm{q} \\ v_\mathrm{e} \end{pmatrix}$	$\begin{pmatrix} i_\mathrm{d} \\ i_\mathrm{q} \\ i_\mathrm{e} \end{pmatrix}$	$\begin{pmatrix} \psi_\mathrm{d} \\ \psi_\mathrm{q} \\ \psi_\mathrm{e} \end{pmatrix}$	$\begin{pmatrix} R_\mathrm{S} & 0 & 0 \\ 0 & R_\mathrm{S} & 0 \\ 0 & 0 & R_\mathrm{R} \end{pmatrix}$	$\begin{pmatrix} 0 & -\omega & 0 \\ \omega & 0 & 0 \\ 0 & 0 & 0 \end{pmatrix}$	$\begin{pmatrix} i_\mathrm{d} \\ i_\mathrm{q} \\ i_\mathrm{e} \end{pmatrix} \mapsto \begin{pmatrix} \psi_\mathrm{d} \\ \psi_\mathrm{q} \\ \psi_\mathrm{e} \end{pmatrix}$
IM	$\begin{pmatrix} v_\mathrm{Sd} \\ v_\mathrm{Sq} \\ 0\mathrm{V} \end{pmatrix}$	$\begin{pmatrix} i_\mathrm{Sd} \\ i_\mathrm{Sq} \\ i_\mathrm{Rd} \end{pmatrix}$	$\begin{pmatrix} \psi_\mathrm{Sd} \\ \psi_\mathrm{Sq} \\ \psi_\mathrm{Rd} \end{pmatrix}$	$\begin{pmatrix} R_\mathrm{S} & 0 & 0 \\ 0 & R_\mathrm{S} & 0 \\ 0 & 0 & R_\mathrm{R} \end{pmatrix}$	$\begin{pmatrix} 0 & -\omega_\mathrm{S} & 0 \\ \omega_\mathrm{S} & 0 & 0 \\ 0 & 0 & 0 \end{pmatrix}$	$\begin{pmatrix} i_\mathrm{Sd} \\ i_\mathrm{Sq} \\ i_\mathrm{Rd} \end{pmatrix} \mapsto \begin{pmatrix} \psi_\mathrm{Sd} \\ \psi_\mathrm{Sq} \\ \psi_\mathrm{Rd} \end{pmatrix}$

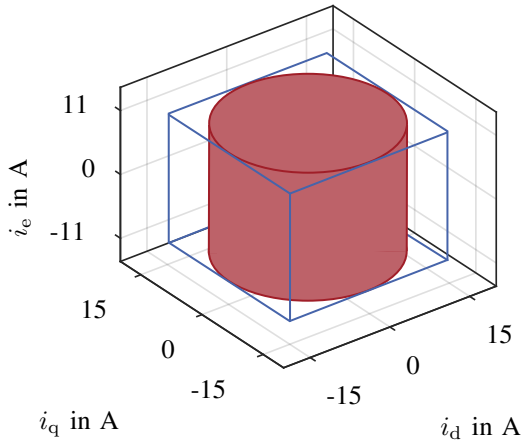

Fig. 3. Domain of f_ψ (red) and outline of grid G_i (blue) for the EESM

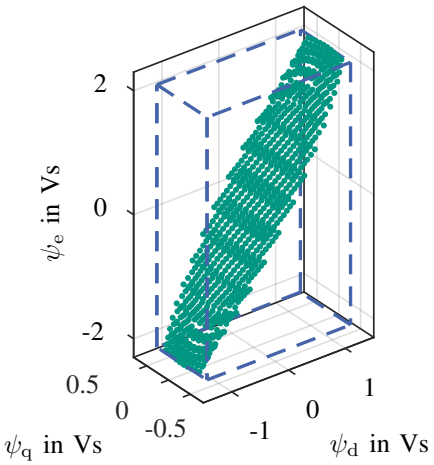

Fig. 4. Point cloud C_ψ and outline of a typical grid in flux space

that the transformation angle for the RFO has to be calculated separately by means of an additional differential equation (current model of IM). By using the respective values from Table I both machines can be modeled with the same block diagram in Fig. 2. Hence it is described as the generalized machine model.

Thereby all magnetic couplings are contained in the flux map. As the nonlinearities are caused by material properties, they appear similarly across all machine types. Thus the nonlinearities can be treated identical for all kinds of machines if precise inverse flux maps can be calculated. In this paper such an inversion algorithm is derived, which enables the adaption of the known PMSM simulation models, HIL-systems and MPC-algorithms for IM and EESM. Additionally, unified control schemes are possible that can operate for any machine type as long as the corresponding inverse flux map is provided [6].

Machine models with higher dimensionality are possible. This is the case for the IM in stator oriented reference frame which requires a four dimensional inverse flux map.

III. Modeling of Nonlinear Effects with Flux Maps

As shown above the nonlinear characteristics of an electric machine can be described as

$$f_\psi : \left(\underline{i},\ \underline{p} \right) \mapsto \underline{\psi} \tag{10}$$

where $\underline{i},\ \underline{\psi} \in \mathbb{R}^n$ are vectors containing the respective current and flux components and n depends on the machine type. The vector $\underline{p} \in \mathbb{R}^m$ contains m additional parameters that affect the magnetics such as rotor position, speed or temperature.

Since an analytical representation of f_ψ with the required accuracy would be to complex, the function is approximated with a map. To do so for each of the n current components an equidistant grid vector

$$I_k = \{i_{k,\min} = i_{\mathrm{k},1}, i_{\mathrm{k},2}, \cdots i_{k,N_k} = i_{k,\max}\} \tag{11}$$

is defined. The cartesian product

$$G_\mathrm{i} = I_1 \times \cdots \times I_n \subset \mathbb{R}^n \tag{12}$$

gives the set of all vectors that result from combining the elements of the grid vectors in order. G_i is called a grid as its elements are arranged in an n-dimensional grid pattern if interpreted as points in space.

The minimum and maximum value of each grid vector have to be chose such that the domain of f_ψ is completely covered. The domain is given by the set of all points in the current state space that can occur during operation. For the EESM the current limit defines the domain as a cylinder which is shown in Fig. 3 in red. The outline of the respective grid G_i is displayed in blue.

Analogously a second grid $G_\mathrm{p} \subset \mathbb{R}^m$ is defined for the arguments $\underline{p}$. The set of all combinations of $\underline{i}_j \in G_\mathrm{i}$ and $\underline{p}_k \in G_\mathrm{p}$ is expressed as the cartesian product

$$G_{\mathrm{i,p}} = G_\mathrm{i} \times G_\mathrm{p}. \tag{13}$$

For each element in $G_{\mathrm{i,p}}$ the respective flux vector is determined by measurement or finite element analysis and stored in the map.

The set C_ψ of all flux vectors stored in the map is an approximation of the co-domain of f_ψ. As an example C_ψ of an EESM is shown as a point cloud in Fig 4. Due to the magnetic coupling between d- and e-axis a strong correlation between the two components is visible in the cloud.

Flux values in between the grid points in current space can be interpolated via various methods. For real-time applications linear interpolations is used due to its low requirements in computing time. During the inverting procedure a higher order interpolation method is used which has the benefit of a continuous derivative.

As an example an excerpt of an EESM flux map is shown in Fig. 5 for several fixed values of i_e. The flux map was obtained by measurement. More information about the machine is given

in section V. All EESM examples shown in this paper refer to the same data set.

IV. Calculation of the Inverse Flux Map

In the flux map only the relation between current and flux needs to be inverted. The parameters $\underline{p}$ are known variables which are determined for each time-step by measurement or mechanical and thermal models. Thus, the inverse flux map is an approximation of the function

$$f_{\psi}^{-1} : \left(\underline{\psi},\ \underline{p} \right) \mapsto \underline{i}. \tag{14}$$

For the inversion process this can be interpreted as inverting a separate flux map for every $\underline{p}_k \in G_{\mathrm{p}}$. The inversion procedure is divided into four consecutive parts. First the invertibility of the flux map is ensured. In the second step a suitable grid for the inverse flux map in calculated before the respective current values are determined. Subsequently the inverse flux map is validated in the final step.

A. Check for Invertibility

According to the inverse function theorem a sufficient condition for invertibility of a vector-valued function f of several variables $\underline{x}$ in a neighborhood of $\underline{x}_0$ is given if the jacobian determinant of f at $\underline{x}_0$ is non-zero [7].

Applied to the flux map the statement

$$\det \left(\frac{\partial f_{\psi}(\underline{i}, \underline{p})}{\partial \underline{i}} \right) \neq 0 \tag{15}$$

has to be ensured for all $\underline{i}$ and $\underline{p}$ in the map which can only be done by approximation. To do so the jacobian is numerically approximated by central finite differences for each grid-point in $G_{\mathrm{i,p}}$ and the determinant is calculated. Subsequently the sign is checked for two reasons. First, numerical values are never exactly zero even if the non-approximated function was zero in the same point. Second, the jacobian determinant could become zero in between grid-points which would express itself as a positive and a negative value at neighboring points. Thus the flux map is assumed to be invertible if the sign of the jacobian determinant in all grid-points is identical.

A proof that every two-dimensional flux map is invertible can be found in [3]. A generalization of the proof for higher dimensional flux maps is not known to the author. It can be mentioned though that every flux map the method has been tried on has been invertible except for cases where measurement artifacts such as outliers, strong noise or large interpolation or extrapolation errors in areas of missing data were present.

B. Definition of a Suitable Grid in Flux Space

Compared to f_{ψ}, domain and co-domain swap roles in the inverse mapping. Hence a grid $G_{\psi} \subset \mathbb{R}^n$ for the argument $\underline{\psi}$ needs to be defined. The grid G_{p} does not change in the inversion process and thus the full grid is given by

$$G_{\psi,\mathrm{p}} = G_{\psi} \times G_{\mathrm{p}}. \tag{16}$$

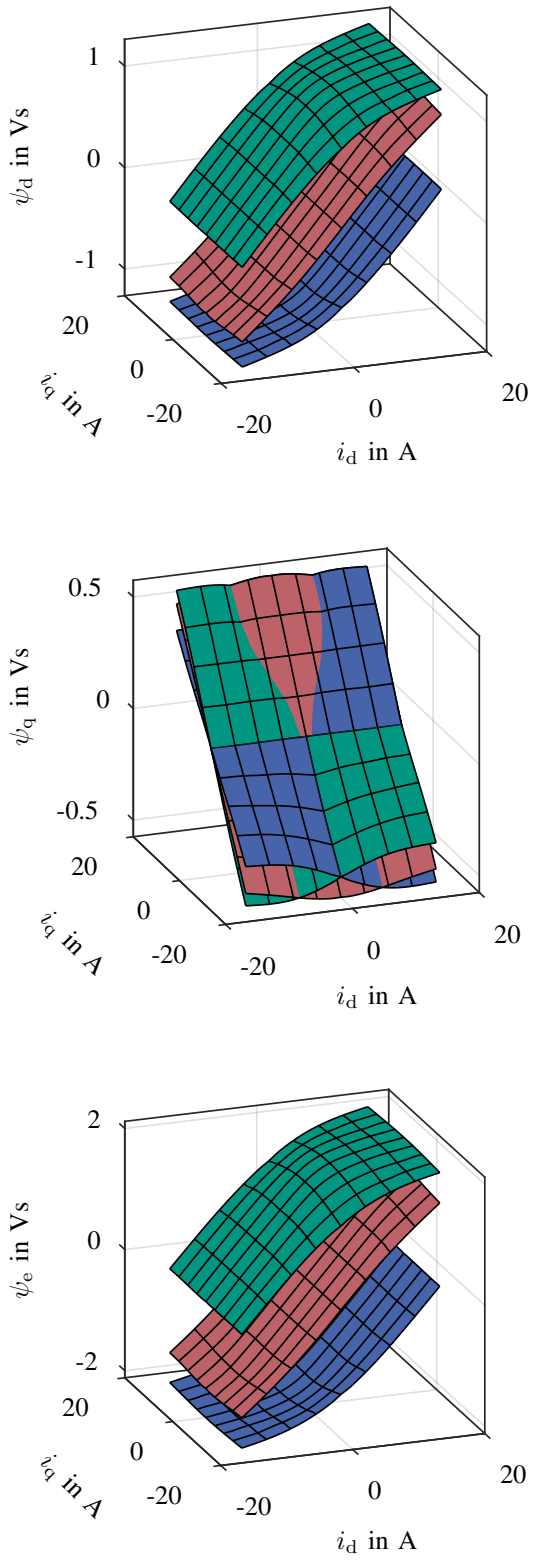

Fig. 5. Excerpt of an EESM flux map for $i_{\mathrm{e}} = -11\mathrm{A}$ (blue), $i_{\mathrm{e}} = 0\mathrm{A}$ (red) and $i_{\mathrm{e}} = 11\mathrm{A}$ (green)

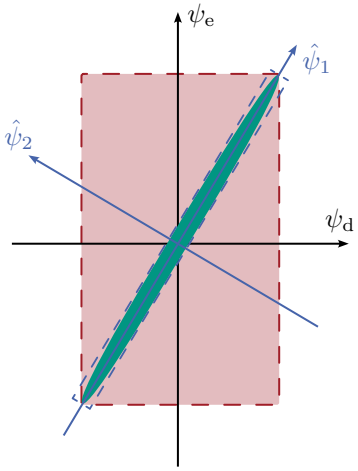

Fig. 6. Overhead and orientation of $S_{\hat{\psi}}$ in 2D view

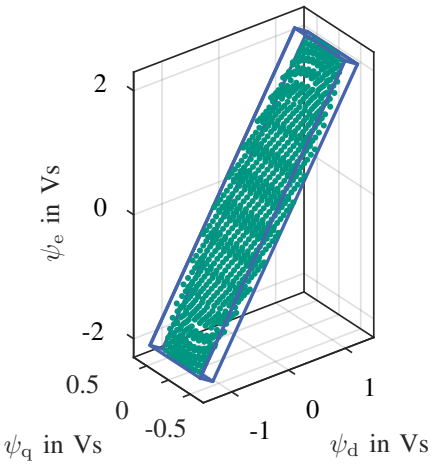

Fig. 7. Point cloud C_ψ and outline of optimized grid in $\hat{\psi}$

By increasing the number of dimensions in existing, two-dimensional inversion algorithms, a grid is defined in orientation along the coordinate axis as indicated in Fig. 4. A major part of the grid points would not hold any values of C_ψ and can be seen as overhead. In the example of the EESM this becomes clear in the 2D view in Fig. 6 where the overhead is marked as red area. Taking the third dimension into account, 94% of the grid points are overhead. The remaining 6% of grid points lead to a rough approximation of the inverse mapping with large interpolation errors. To achieve a precise and resource efficient inverse map the overhead must be greatly reduced.

This is achieved by orienting the grid in a way that C_ψ is enclosed as tightly as possible. To do so, an auxiliary coordinate system $S_{\hat{\psi}}$ is defined as shown in Fig. 6 along the axes of which the grid G_ψ is set up as shown in Fig. 7. A suitable orientation of $S_{\hat{\psi}}$ can be found by calculating the principal components [8].

For that, the covariance matrix $\underline{K}_\psi$ of C_ψ is calculated

$$\underline{K}_\psi = \left(\mathrm{cov}(\psi_j, \psi_k)\right)_{j,k=1\cdots n} \tag{17}$$

where ψ_j and ψ_k are the j-th and k-th element in the vectors $\underline{\psi} \in C_\psi$. Therefore the covariance is estimated as

$$\mathrm{cov}(\psi_j, \psi_k) = \frac{1}{N-1}\sum_{l=1}^{N}(\psi_{j,l} - \mu_{\psi_\mathrm{j}})(\psi_{k,l} - \mu_{\psi_\mathrm{k}}) \tag{18}$$

with N being the number of elements in C_ψ and μ_{ψ_j}, μ_{ψ_k} being the mean values of the respective flux components. By calculating the covariance between flux components information about all magnetic couplings is contained in $\underline{K}_\psi$.

The principal components are obtained as the eigenvectors of $\underline{K}_\psi$. As they form an orthogonal base that is oriented along the direction of the covariance in the dataset and thus along the magnetic couplings the principal components are the ideal choice for $S_{\hat{\psi}}$. The resulting orientation of the grid is shown in Fig. 7 for the EESM. This approach can be applied to any number of dimensions.

The transformation matrices $\underline{T}_{\hat{\psi}\to\psi}$ and $\underline{T}_{\psi\to\hat{\psi}}$ are used to convert a vector's coordinate representation between the two systems.

$$\underline{\psi} = \underline{T}_{\hat{\psi}\to\psi} \cdot \underline{\hat{\psi}} \tag{19}$$

$$\underline{\hat{\psi}} = \underline{T}_{\psi\to\hat{\psi}} \cdot \underline{\psi} \tag{20}$$

$\underline{T}_{\hat{\psi}\to\psi}$ contains the eigenvectors of $\underline{K}_\psi$ and $\underline{T}_{\psi\to\hat{\psi}}$ is the corresponding inverse matrix. In the inverse flux map the current values are stored with reference to the system $S_{\hat{\psi}}$. This makes it necessary to transform a vector $\underline{\psi}$ by means of (20) before the corresponding current values can be obtained by the look-up operation.

C. Calculation of Current Values

To find the current vectors $\underline{i}_{j,k}$ that need to be stored in the inverse map for the grid points $(\,\underline{\hat{\psi}}_j,\ \underline{p}_k\,) \in G_{\psi,\mathrm{p}}$ the nonlinear system of equations

$$f_\psi(\,\underline{i}_{j,k},\ \underline{p}_k\,) \stackrel{!}{=} \underline{T}_{\hat{\psi}\to\psi} \cdot \underline{\hat{\psi}}_j \tag{21}$$

must be solved for every $\underline{i}_{j,k}$. In the present work this was done by using the trust-region-dogleg-algorithm implemented in MATLAB's "fsolve" function.

To execute the algorithm for each $\underline{i}_{j,k}$ a start value $\underline{i}^0_{j,k}$ has to be provided. Beginning at $\underline{i}^0_{j,k}$ the algorithm varies the current vector in an iterative procedure until convergence towards the given flux vector is reached. Therefore the flux map f_ψ is used with a modified version of the akima interpolation which is in MATLAB available under the name "makima". Convergence can be accelerated if a start point near the solution is chosen.

To find suitable start points the following procedure has been used. For a given current grid-point in G_i the respective flux vector is known by f_ψ. If the nearest flux grid-point in G_ψ is found, the current grid-point can be assumed to be close to

TABLE II
CHARACTERISTIC DATA OF THE FESM

Symbol	Meaning	Value
$P_{\max}$	maximum Power	5.9 kW
$i_{\mathrm{s,max}}$	maximum stator current	15 A
$i_{\mathrm{e,max}}$	maximum excitation current	13 A
$U_{\mathrm{S,DC}}$	nominal stator DC link voltage	400 V
$n_{\max}$	maximum speed	5000 rpm
$M_{\max}$	maximum Torque	40 Nm

the solution of (21) for that flux grid-point and is hence used as start value.

D. Validation of the Inverse Flux Map

In the validation step the inverse map's quality is checked. Therefore, the fact that the function composition of a function and its inverse equals the identity function is used. For each element in a set of test points $(\underline{i}_j, \underline{p}_k) \in P$ the error can be calculated by

$$e_{j,k} = || \, f_\psi^{-1}(\, f_\psi(\, \underline{i}_j, \, \underline{p}_k \,), \, \underline{p}_k \,) - \underline{i}_j \, || \tag{22}$$

If P is chosen to be the grid $G_{\mathrm{i,p}}$ with additional subdivisions, the error in between the grid points as a result of the interpolation can be evaluated as well. The distribution of the error over all test points can than be analyzed.

V. INVERSION RESULTS

In this section the inversion results of an EESM's and an IM's flux maps are presented. The algorithm has been tested extensively on both FEA and measured datasets. As measured flux maps are subject to noise and measurement errors they tend to produce lager inversion errors than perfectly smooth flux maps from FEA. To proof the capability of the algorithm both flux maps presented in this section have been acquired by test bench measurement.

A. Results for the EESM Inverse Flux Map

Characteristic data of the EESM is given in Table II. The same machine has been used as reference in [9] where more information can be found. The test bench used for flux map measurement is described in detail in [6].

The flux map has been identified for stator current amplitudes smaller than 15 A and excitation currents up to 11 A. In the results shown in Fig. 5 the measurement data was interpolated and extrapolated to a grid of 25 point in each dimension. No further post processing has been applied.

The corresponding inverse flux map is shown in Fig. 8 for several, constant values of the excitation flux ψ_{e}. The computation time was 117s using a *AMD Ryzen 7 PRO 5850U* without parallel computing. By use of the optimal oriented grid the share of non-overhead points was increased by a factor of 8 from 6% to 48%. To compensate for that the number of grid points in G_ψ was doubled compared to G_{i} in order to have the same amounts of non-overhead grid-points in both f_ψ and f_ψ^{-1}.

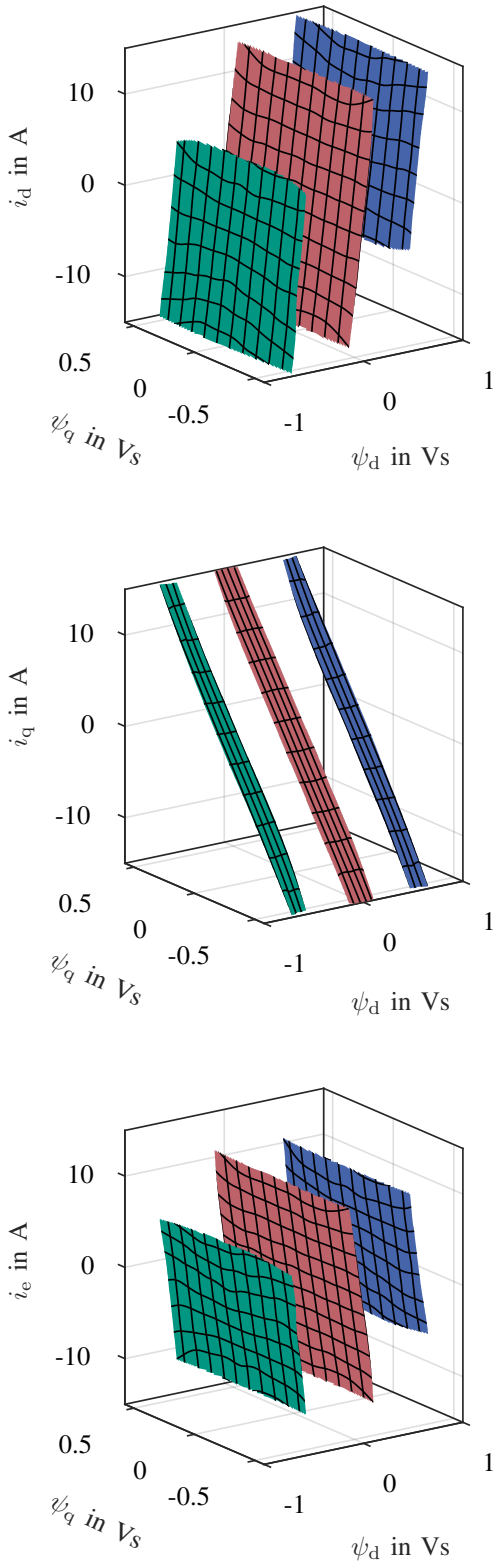

Fig. 8. Inverse flux map of the EESM for $\psi_{\mathrm{e}} = 1$Vs (blue), $\psi_{\mathrm{e}} = 0$Vs (red) and $\psi_{\mathrm{e}} = -1$Vs (green)

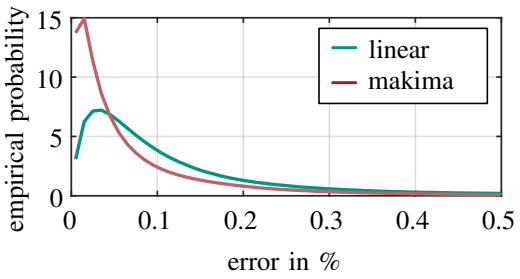

Fig. 9. Distribution of the error in scale of a probability density function

The error was calculated according to the validation procedure using a test grid P with 10 additional subdivisions. The error distribution of the test points is shown in an empirical density function in Fig. 9. The error is given in percentage of the maximum current value of 15 A. The test has been carried out for both linear and "makima" interpolation. The mean value amounts to 0.15% for linear and 0.1% for the "makima" interpolation. Thus the calculated map is a precise approximation of the inverse mapping. The cause of the remaining error is assumed to be interpolation error as it changes with the interpolation method and decreases if the number of grid points in G_{i} and G_{ψ} is increased.

For comparison the inversion is performed again using a grid as indicated in Fig. 4 without the optimized orientation. For comparability the number of grid-points in G_{ψ} is kept the same as above. Performing the same test with linear interpolation the mean error increases by more than tenfold to 1.7%. By increasing the number of grid-points by a factor of 17 the mean error decreases to 0.3% which is still twice as large as with the optimized grid. This underlines the effectiveness of the optimized grid concerning accuracy and resource efficiency.

B. Results for the IM Inverse Flux Map

The measured IM flux maps are shown in Fig.10. A *Siemens 1LE1592-1EB42-1AF4* was used of which some characteristics are summarized in Table III. Details about the test bench and the measurement method can be found in [10], as the same data was used. The flux maps have been interpolated and extrapolated to a grid of 25 points per dimension without further post processing.

Without the optimized grid orientation only 4% of grid point are used, with the optimized grid orientated along $S_{\hat{\psi}}$ that number increases to 54%. Thus the number of grid points in

TABLE III
CHARACTERISTIC DATA OF THE IM

Symbol	Meaning	Value
P_{N}	Nominal Power	22 kW
$i_{\mathrm{S,N}}$	Nominal stator current	45 A
U_{N}	Nominal voltage	380 V
n_{N}	Nominal speed	1500 rpm

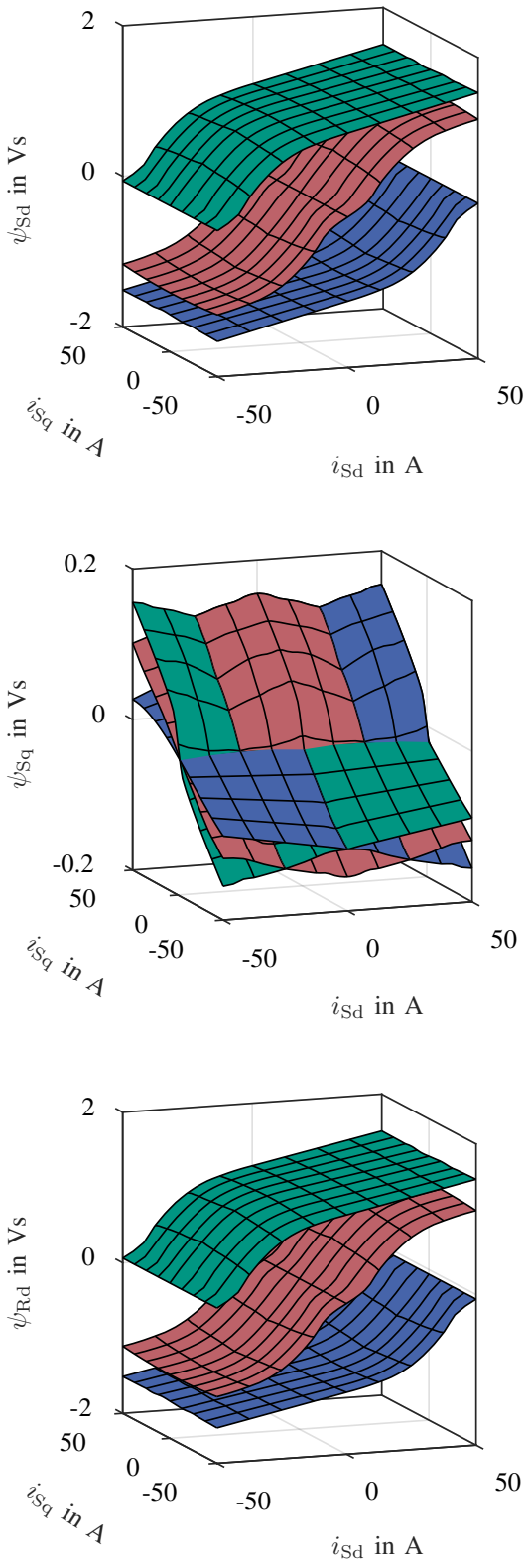

Fig. 10. Flux map of the IM for $i_{\mathrm{Rd}} = -50$A (blue), $i_{\mathrm{Rd}} = 0$A (red) and $i_{\mathrm{Rd}} = 50$A (green)

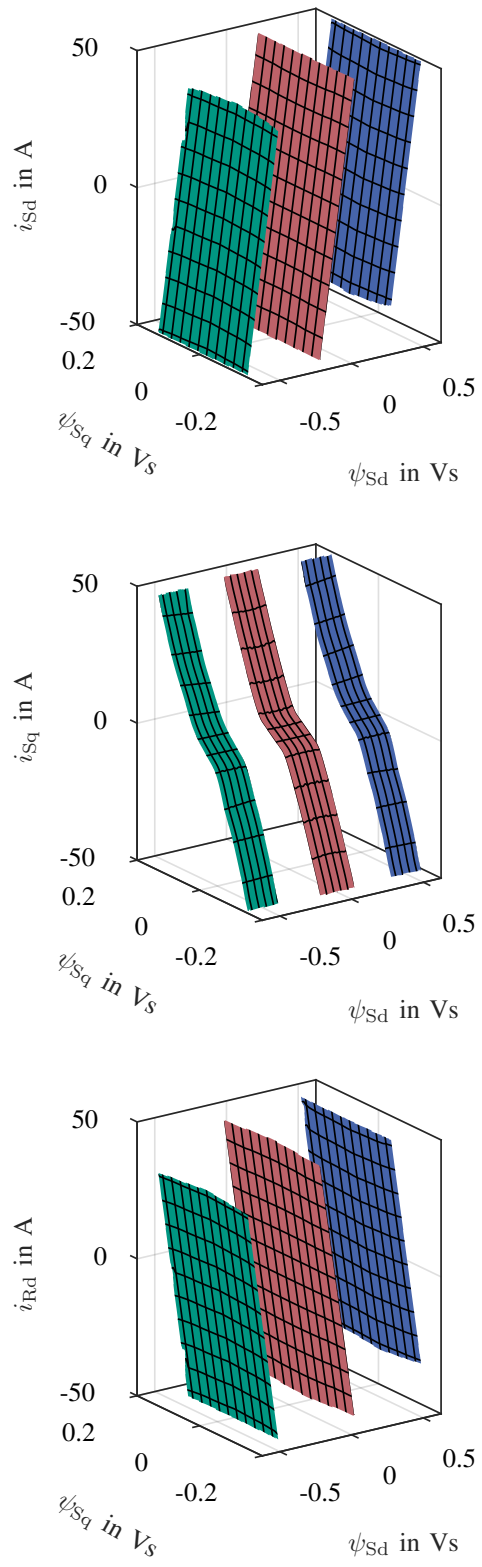

Fig. 11. Inverse flux map of the IM for $\psi_{\mathrm{Rd}} = 0.5\mathrm{Vs}$ (blue), $\psi_{\mathrm{Rd}} = 0\mathrm{Vs}$ (red) and $\psi_{\mathrm{Rd}} = -0.5\mathrm{Vs}$ (green)

G_ψ was doubled compared to G_{i} to have the same number of non-overhead points in f_ψ and f_ψ^{-1}. The resulting inverse flux map is shown in Fig. 11. The validation with 10 additional subdivisions and linear interpolation results in a mean error of 0.34%.

VI. Conclusion

In this paper a method for inverting n-dimensional flux maps was described, which is an essential pre-condition to achieve uniform, nonlinear modeling and controls across different machine types. For that the concept of a generalized machine model was introduced. A criterion for checking the invertibility of a flux map was derived. The required amount of grid points for a precise representation of the inverse map was greatly reduced by using an optimal oriented grid in flux space.

The algorithm has been tested extensively on FEA-simulated maps as well as on measured datasets. The precision and resource efficiency were demonstrated on two measured datasets. The presented method enables precise machine modeling using higher dimension inverse flux maps which can be used under hard real time conditions.

References

[1] X. Chen, J. Wang, B. Sen, P. Lazari, and T. Sun, "A high-fidelity and computationally efficient model for interior permanent-magnet machines considering the magnetic saturation, spatial harmonics, and iron loss effect," *IEEE Transactions on Industrial Electronics*, vol. 62, no. 7, pp. 4044–4055, 2015.

[2] J. A. Choi and J. S. Lee, "Development of a pmsm hil system with an inverse flux model," in *2022 IEEE 5th Student Conference on Electric Machines and Systems (SCEMS)*, 2022, pp. 1–4.

[3] J. Richter, T. Gemaßmer, and M. Doppelbauer, "Predictive current control of saturated cross-coupled permanent magnet synchronous machines," in *2014 International Symposium on Power Electronics, Electrical Drives, Automation and Motion*, 2014, pp. 830–835.

[4] S. Wendel, P. Karamanakos, A. Dietz, and R. Kennel, "Flux linkage-based model predictive current control for nonlinear pmsm drives," in *IECON 2020 The 46th Annual Conference of the IEEE Industrial Electronics Society*, 2020, pp. 3051–3056.

[5] S. Decker, M. Brodatzki, B. Bachowsky, B. Schmitz-Rode, A. Liske, M. Braun, and M. Hiller, "Predictive trajectory control with online mtpa calculation and minimization of the inner torque ripple for permanent-magnet synchronous machines," *Energies*, vol. 13, no. 20, 2020.

[6] J. Stoss, L. Geier, A. Karayel, A. Liske, and M. Hiller, "Unified predictive flux control for eesm, im, pmsm and srm," in *2023 IEEE Energy Conversion Congress and Exposition (ECCE)*, 2023.

[7] G. Paltineanu, "Differential calculus for engineers," Singapore, pp. 159–160, 2022.

[8] R. Vidal, Y. Ma, and S. Sastry, "Generalized principal component analysis," [2016]. [Online]. Available: https://doi.org/10.1007/978-0-387-87811-9

[9] P. Winzer, "Steigerung von drehmoment und wirkungsgrad bei synchronmaschinen durch nutzung der magnetischen asymmetrie," Ph.D. dissertation, Karlsruher Institut für Technologie (KIT), 2017.

[10] J. Stoss, A. Karayel, L. Geier, A. Liske, and M. Hiller, "Identification of rotor and stator flux linkage maps of squirrel cage induction motors based on identification of rotor time constant maps," in *25th European Conference on Power Electronics and Applications*, 2023.